Focus Section: Arctic and Antarctic Seismology

Seismic Monitoring of Permafrost in Svalbard, Arctic Norway

Julie Albaric[*1,2], Daniela Kühn[2], Matthias Ohrnberger[3], Nadège Langet[2], Dave Harris[4], Ulrich Polom[5], Isabelle Lecomte[2,6], and Gregor Hillers[7]

Abstract

We analyze data from passive and active seismic experiments conducted in the Adventdalen valley of Svalbard in the Norwegian Arctic. Our objective is to characterize the ambient wavefield of the region and to investigate permafrost dynamics through estimates of seismic velocity variations. We are motivated by a need for early geophysical detection of potentially hazardous changes to permafrost stability. We draw upon several data sources to constrain various aspects of seismic wave propagation in Adventdalen. We use *f-k* analysis of five years of continuous data from the Spitsbergen seismic array (SPITS) to demonstrate that ambient seismic noise on Svalbard consists of continuously present body waves and intermittent surface waves appearing at regular intervals. A change in wavefield direction accompanies the sudden onset of surface waves when the average temperature rises above the freezing point, suggesting a cryogenic origin. This hypothesis is supported further by our analysis of records from a temporary broadband network, which indicates that the background wavefield is dominated by icequakes. Synthetic Green's functions calculated from a 3D velocity model match well with empirical Green's functions constructed from the recorded ambient seismic noise. We use a shallow shear-wave velocity model, obtained from active seismic measurements, to estimate the maximum depth of Rayleigh wave sensitivity to changes in shear velocity to be in the 50–100 m range. We extract seasonal variations in seismic velocities from ambient noise cross-correlation functions computed over three years of SPITS data. We attribute relative velocity variations to changes in the ice content of the shallow (2–4 m depth) permafrost, which is sensitive to seasonal temperature changes. A linear decreasing trend in seismic velocity is observed over the years, most likely due to permafrost warming.

Cite this article as Albaric, J., D. Kühn, M. Ohrnberger, N. Langet, D. Harris, U. Polom, I. Lecomte, and G. Hillers (2021). Seismic Monitoring of Permafrost in Svalbard, Arctic Norway, *Seismol. Res. Lett.* **92**, 2891–2904, doi: 10.1785/0220200470.

Supplemental Material

Introduction

Warming of permafrost in polar territories is a major concern associated with the overall change of the global climate system, especially because of its potential for greenhouse gases emission (Anisimov, 2007; Schaefer *et al.*, 2014). Monitoring its dynamic properties is thus essential. Permafrost is thermally defined as ground that remains at or below 0°C for at least two consecutive years (Williams and Smith, 1989). The top of the permafrost, called the active layer, is subject to summer thawing and winter freezing. Below this, the permafrost shows seasonal subzero temperature variations down to the depth of zero annual amplitude (e.g., Isaksen *et al.*, 2007). The pore space of permafrost can be filled with a variable proportion of gas, ice, and water, depending on several factors such as temperature, pore size and shape, nature of the water, salinity, and stress state (e.g., Timur, 1968; Zimmerman and Michael, 1986; Stemland *et al.*, 2020).

Seismic monitoring is one of the most suitable methods for detecting changes in permafrost dynamic properties because seismic velocities are particularly sensitive to the ice content of the ground and increase, for example, when water in the pore medium is freezing (e.g., Timur, 1968; Zimmerman and Michael, 1986; LeBlanc *et al.*, 2004; Dou and Ajo-Franklin, 2014; Dou *et al.*, 2016; Stemland *et al.*, 2020). As temperature decreases below 0°C, interstitial water freezes, first within larger pore spaces and then within smaller ones, resulting in a gradual increase in seismic velocities (Timur, 1968;

1. Chrono-environnement UMR6249, CNRS, University of Bourgogne Franche-Comté, F-25000, Besançon, France, https://orcid.org/0000-0001-7275-554X (JA); 2. Applied Seismology, NORSAR, Kjeller, Norway, https://orcid.org/0000-0002-2448-1510 (DK); https://orcid.org/0000-0002-3203-7604 (NL); https://orcid.org/0000-0002-3316-535X (IL); 3. Institute of Geosciences, University of Potsdam, Germany, https://orcid.org/0000-0003-1068-0401 (MO); 4. Deschutes Signal Processing LLC, Maupin, Oregon, U.S.A.; 5. Leibniz Institute for Applied Physics, Hannover, Germany; 6. Department of Earth Science, University of Bergen, Bergen, Norway; 7. Institute of Seismology, University of Helsinki, Helsinki, Finland, https://orcid.org/0000-0003-2341-1892 (GH)

*Corresponding author: julie.albaric@univ-fcomte.fr

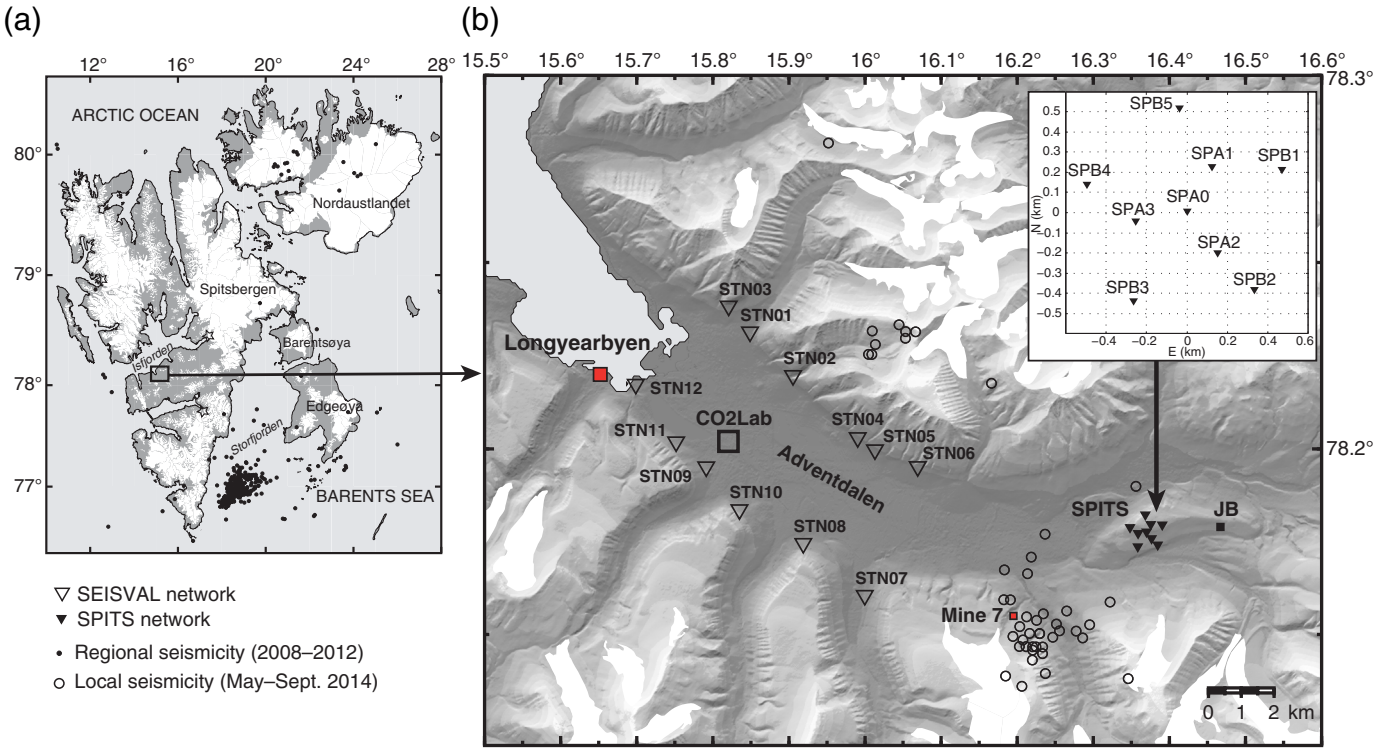

Figure 1. Overview on the study area. (a) Map of the Svalbard Archipelago. (b) Map of the Adventdalen area. The location of the CO_2Lab is indicated by an open square. The SEISVAL seismic network and the Spitsbergen seismic array (SPITS) array are indicated by open and black filled triangles, respectively. The names and relative locations of the SPITS array stations are indicated in the upper right corner inset. Black filled circles in (a) correspond to regional seismicity between 2008 and 2018 (Pirli *et al.*, 2013) and empty circles in (b) to local events located in this study. White areas correspond to glaciers (mapped using data; see Data and Resources, Raup *et al.*, 2007). JB refers to the Janssonhaugen temperature borehole (Isaksen *et al.*, 2001). The color version of this figure is available only in the electronic edition.

Zimmerman and Michael, 1986; LeBlanc *et al.*, 2004). This phenomenon has been observed in the active layer by several studies analyzing seasonal velocity change based on ambient seismic noise monitoring (James *et al.*, 2017, 2019; Kula *et al.*, 2018; Köhler and Weidle, 2019) and repeated active seismic experiments (Stemland *et al.*, 2020). In addition, velocity contrasts associated with unfrozen interstitial water have been detected below the active layer, in particular through *P*- and *S*-wave seismic tomography (LeBlanc *et al.*, 2004) and active surface wave surveys (Dou and Ajo-Franklin, 2014). For example, the laboratory analysis from Zimmerman and Michael (1986) indicated an increase of *P*- and *S*-wave velocity of more than 10% in some permafrost sediment core samples due to ice saturation increasing between −5°C and −15°C.

In this article, we investigate changes in the properties of permafrost related to seasonal temperature changes. We estimate seismic velocity variations using three years of ambient seismic noise recorded on Svalbard, Norway (Fig. 1). The Svalbard archipelago is located in the Arctic Ocean on the northwestern margin of the Barents Sea shelf (e.g., Bungum *et al.*, 1991). The area exhibits regular seismic activity comprising tectonic and glacial events (e.g., Köhler *et al.*, 2012; Pirli *et al.*, 2013). Our research concentrates on the Adventdalen valley close to the town of Longyearbyen, located on Spitsbergen island. The geological and tectonic characteristics of Adventdalen were studied in detail, in particular in association with the carbon capture and storage research carried out by the Longyearbyen CO_2Lab of the University Centre in Svalbard (UNIS; Braathen *et al.*, 2012; Senger *et al.*, 2014; Olaussen *et al.*, 2019). Drill cores at the location of the CO_2Lab indicated 60–70 m of Holocene gravel and sand followed by a succession of sandstones, silts, and shales comprising the Cretaceous formations of the Adventalen group overlying a sandstone unit targeted as a potential CO_2 reservoir at ∼670 m depth. Microseismic monitoring at the CO_2Lab was described in Oye *et al.* (2010, 2013), Kühn *et al.* (2014), and Harris *et al.* (2017).

Permafrost on Spitsbergen is overlain by a seasonally unfrozen active layer of about 0.8 to ∼2 m thickness and underlies at least 90% of the land surface not covered by glaciers (Humlum *et al.*, 2003; Christiansen *et al.*, 2010; Westermann *et al.*, 2010). The total permafrost thickness was estimated to be 120–160 m at the CO_2Lab (Braathen *et al.*, 2012) and 220 m within the Janssonhaugen temperature borehole (JB in Fig. 1; Isaksen *et al.*, 2001). Permafrost warming on Svalbard has already been detected and will likely continue

over the next century (Isaksen *et al.*, 2007; Seneviratne *et al.*, 2016). Thus, seismic monitoring of permafrost resilience or vulnerability, respectively, is crucial.

The analysis of Green's functions (or cross-correlation functions [CCFs]) constructed from the ambient wavefield through seismic interferometry (e.g., Shapiro and Campillo, 2004; Snieder, 2004; Hadziioannou *et al.*, 2009) has become a standard tool in seismology for imaging (e.g., Shapiro *et al.*, 2005; Roux *et al.*, 2011; Lehujeur *et al.*, 2018) and monitoring temporal changes in seismic velocity (e.g., Snieder *et al.*, 2002; Sens-Schönfelder and Wegler, 2006; Brenguier *et al.*, 2008; Hillers *et al.*, 2015). Techniques measuring interstation noise-correlation functions allow for the tracking of variations in propagation characteristics over time and distance scales governed by the coherent parts of the ambient wavefield.

We processed seismic data from passive and active monitoring systems (Fig. 1): a permanent small-aperture array (Spitsbergen seismic array [SPITS]), a local temporary network (SEISVAL), and an active *S*-wave seismic experiment at the CO_2Lab. The results of the active seismic experiment allowed for improved estimates of the shallow velocity structure of Adventdalen and served for event location and Rayleigh wave sensitivity analysis. SPITS and SEISVAL seismic recordings were both used to characterize the ambient wavefield. SEISVAL CCFs were compared with synthetics computed through a large-scale 3D velocity model of the Adventdalen to improve our interpretation of scattered wave propagation in the valley. From the SPITS CCFs, we estimated long-term seasonal velocity variations in the permafrost.

Seismic Monitoring Networks in Adventdalen

Permanent seismic array: SPITS

The SPITS array (Fig. 1) is located about 10 km southeast of Longyearbyen on an outcrop of the Helvetiafjellet geological formation, consisting of sandstone, shale, coal, and conglomerate. It was installed by the Norwegian Seismic Array (NORSAR) in 1992 (Mykkeltveit *et al.*, 1992) for seismic monitoring of the archipelago and the Arctic and is today part of the Comprehensive Nuclear-Test-Ban Treaty international monitoring system (Schweitzer *et al.*, 2021). This permanent installation currently consists of nine broadband stations arranged on two concentric circles with 500 m and 1 km diameters, respectively (Güralp CMG-3TB, 100 s - 50 Hz, connected to CMG-DM24 digitizers; Pirli, 2013). Stations record data continuously at 80 Hz on three components, except for three one-component stations (SPA1, SPA2, and SPA3; Fig. 1). The sensors are installed at 6 m depth to be shielded from noise produced by wind and anthropogenic activities. The data are automatically and manually processed by NORSAR for earthquake bulletins (NORSAR, 1971) distributed to national and international data centers.

Temporary broadband network: SEISVAL

The SEISVAL temporary network (Fig. 1) consisted of 12 stations deployed in Adventdalen during summer 2014 (May–September). Six of the sensors were CMG 40 instruments (Güralp, 60 s-50 Hz); the remaining six were Noemax seismometers (Agecodagis, 20 s-50 Hz). The sampling frequency of the Taurus digitizers was set to 100 Hz. Most of the stations were installed on large blocks of rock, in some cases requiring an additional cement base to enhance leveling, in particular for the Noemax sensors. Two stations (STN07 and STN08) were installed on existing concrete bases and one (STN12) inside a cabin. Each sensor was protected with a plastic box insulated with rock wool and sealed to the rock with cement. Most of the stations acquired data during the whole installation period; however, station STN04 stopped recording in mid-June, station STN08 from mid-July to mid-August, and station STN10 did not record data except for a very short period. From spectrograms, it was evident that STN01 was malfunctioning at least during the last period of the deployment.

Active seismic experiment

S-wave reflection and vibroseis downhole experiments. To build a 1D velocity model of the shallow subsurface, vibroseis *S*-wave reflection and downhole experiments were conducted in September 2012 (Oye *et al.*, 2013).

For the *S*-wave reflection experiment, a 100-m-long profile was acquired on a gravel road in the Longyearbyen CO_2Lab area (see CO_2Lab marker on Fig. 1 and P2 seismic line on Fig. S1, available in the supplemental material to this article). The *S*-wave source consisted of an electrodynamically driven linear shaker (Electrodynamic-Vibrator System [ElViS]) mounted below a wheelbarrow frame (Polom, 2006; Polom *et al.*, 2010, 2011) utilizing the Vibroseis method (Crawford *et al.*, 1960). The shaking orientation was perpendicular to the acquisition line to generate horizontally polarized *S*-waves (*SH*). The signals were recorded by 48 horizontal geophones (*SH*-mode, SM6-H 10 Hz) mounted every 2 m on a land streamer. Data were preprocessed using the VISTA 10.028 seismic data processing software (GEDCO Inc., Calgary, Canada). The shallowest 10 m of the profiles were affected by the presence of the road that induced an artificial velocity layer; thus, they were removed from the analysis. Figure 2a depicts a sequence of two-fold stacked raw records from P2, acquired on the main road. FX-deconvolution was applied to reduce wind noise before finite-difference time migration using smoothed stacking velocities. *S*-wave interval velocities derived from the stacking velocities are presented together with the depth-converted final section in Figure 2b. The results indicated low *S*-wave velocities of about ~200 m/s in the upper 50 m, increasing to ~450 m/s at 75 m depth. Because of the limited acquisition line spread of 95 m and wind noise affecting the raw data, the precision of the velocity calculation decreased at greater depth and could not be interpreted.

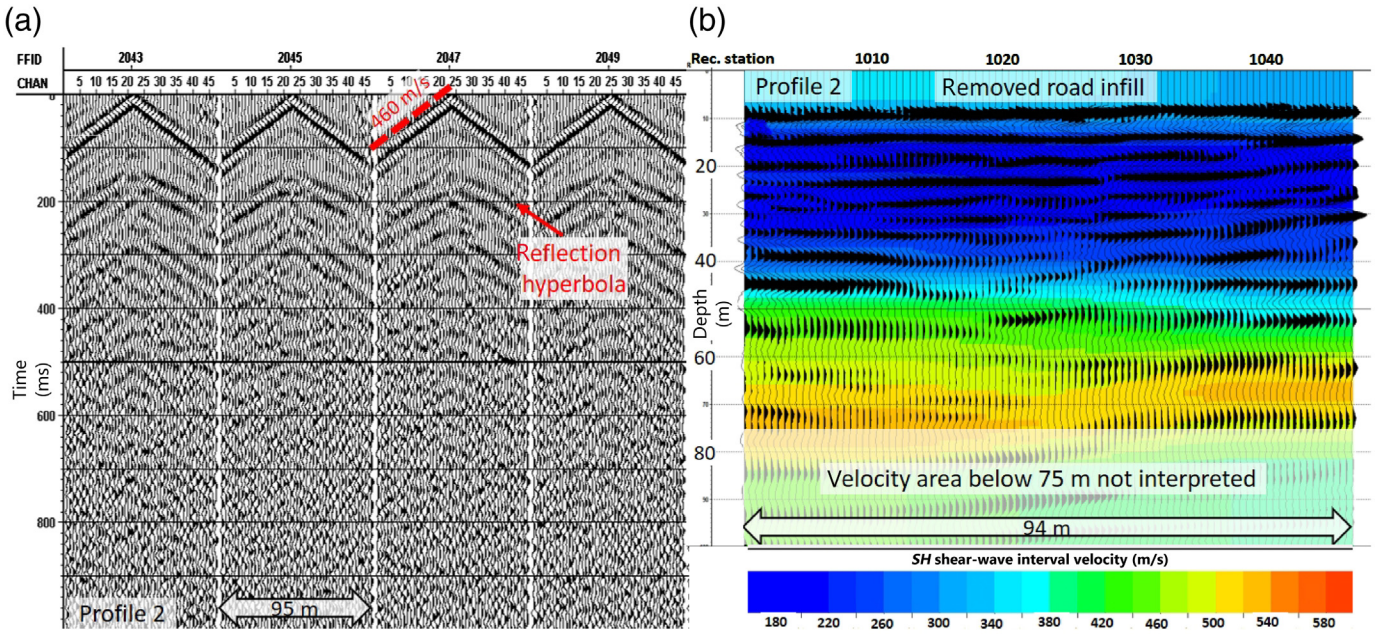

Figure 2. Profile 2 along the main road. (a) Examples of shot records. (b) Final depth-converted finite-difference-migrated time section, with superimposed color-coded *S*-wave interval velocities. The color version of this figure is available only in the electronic edition.

A complementary *S*-wave vibroseis downhole experiment was carried out around observation well Dh3 (Fig. S1b). Dh3 was equipped with a string of five three-component geophones located between 94 and 294 m in depth with a 50 m spacing. The string was connected to a Geometrics GEODE automatic recording system used for continuous passive seismic monitoring (Kühn *et al.*, 2014). The ElViS microvibrator was employed again to generate *SH* and *SV* polarized shear waves at shot points around the well (S1–S11 in Fig. S1). Data processing included adjusting the source timing, a static shift, a vibroseis correlation (Crawford *et al.*, 1960), band-pass filtering between 20 and 85 Hz, and normalizing the traces. The processed data are presented in Figure S2. Results were similar for both *SV* and *SH* source configurations. *P*-wave arrivals could be identified on the vertical components down to the 194 m depth level. Because the *S*-wave onset was visible only at 94 m depth, the *S*-wave arrival was determined by waveform matching on the other geophones. Accordingly, *P*- and *S*-wave velocities were well resolved down to 194 m in depth. The average *P*-wave velocity from the surface to 94 m depth was 1800 m/s (505 m/s for the *S*-wave velocity) and 3571 m/s between 94 and 194 m in depth (1726 m/s for the *S*-wave velocity).

Velocity model building. To construct a near-surface 1D velocity model, results from both the reflection and vibroseis downhole experiments were integrated (Fig. S3a,b). For the *S*-wave model, velocities from the reflection experiment from the surface to 75 m in depth were combined with the velocities extracted from the vibroseis downhole survey for depths between 94 and 194 m. Velocities were linearly interpolated between 75 and 94 m in depth. However, the *S*-wave velocities in the uppermost part of the velocity model may still be overestimated due to the presence of a gravel road. The *P*-wave velocity model was less well constrained, and a value of 1500 m/s was assumed at the surface following Bælum *et al.* (2012). The velocity at 75 m depth was derived from the *S*-wave velocity employing a V_P/V_S ratio of 1,7. For the depth range between 94 and 194 m, the *P*-wave velocity model was based on the downhole experiment results (Figs. S2 and S3b).

Within the scope of the Longyearbyen CO_2Lab project, active seismic experiments were conducted to assess the potential for CO_2 sequestration and to develop a 3D reservoir model for the Adventdalen valley (Bælum *et al.*, 2012; Braathen *et al.*, 2012; Senger *et al.*, 2014). From these measurements, recorded by snow streamer in winter conditions, only *P*-wave velocities were available, focusing on the bedrock succession, especially the proposed reservoir layer. The main feature of the reservoir model was strata dipping toward the southwest by 1°–3°, such that the proposed reservoir layer, situated at 670–970 m in depth below the CO_2Lab, outcropped 15–20 km to the northeast (Bergh *et al.*, 1997; Braathen *et al.*, 2012). From this model, a 3D raytracing model was constructed (see fig. 7 in Lubrano Lavadera *et al.*, 2018). We employed this model for the computation of synthetic Green's functions to resolve potential 3D effects, for example, those caused by topography (see the Modeling CCFs section). The near-surface 1D velocity model was extended to larger depths by merging it with a profile from the 3D raytracing model extracted at the CO_2Lab location (Fig.

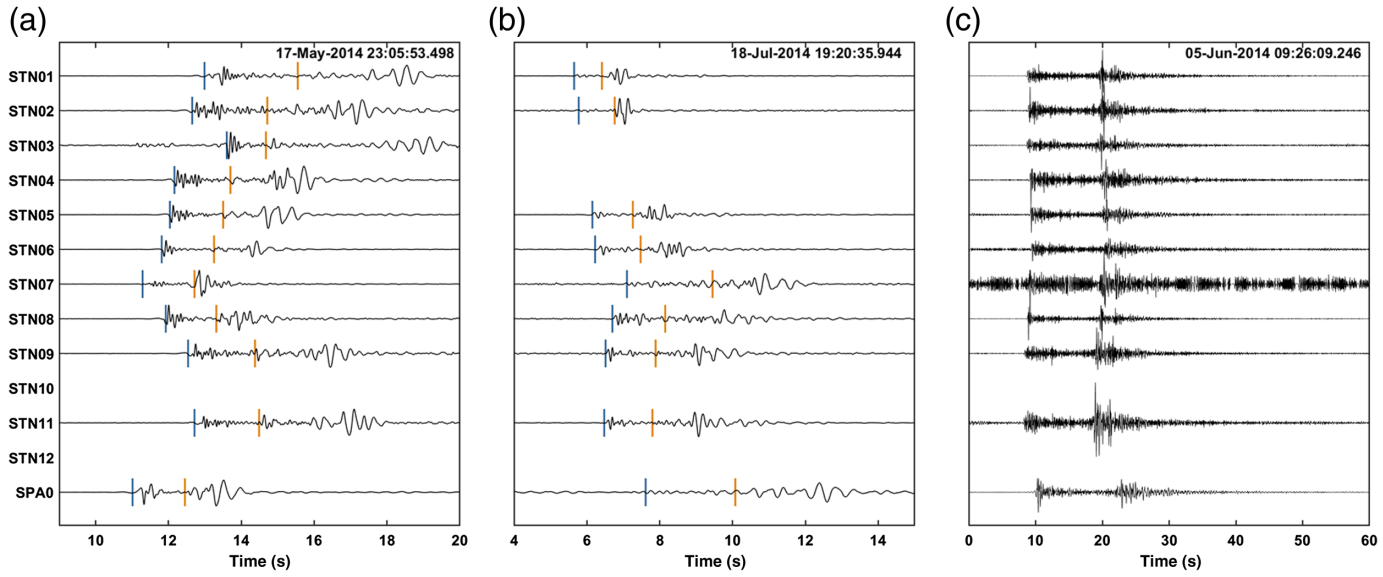

Figure 3. Vertical-component records of (a) a local event located to the southeast with respect to the SEISVAL network; (b) a local event located to the north with respect to the SEISVAL network, and (c) a regional earthquake. Data are filtered between 2 and 20 Hz. In (a) and (b), the blue and orange bars represent the *P*- and *S*-wave picks used for event location, respectively. The color version of this figure is available only in the electronic edition.

S3c,d). We used this composite 1D velocity model as described in the following sections to locate the microseismic events recorded on the temporary broadband network (see the Local microseismicity and icequakes section) and to analyze the influence of *S*-wave velocities on the Rayleigh wave velocity (see the Rayleigh wave sensitivity section).

Characterization of the Ambient Wavefield

Local microseismicity and icequakes

This section assesses the contribution of microseimicity and icequake activity to the ambient wavefield in Adventdalen. In particular, we investigated the benefit of installing the SEISVAL temporary network to enhance the detection capacity for local events. Because of the small aperture of the SPITS array, only the central station (SPA0) was included in the analysis. The event detection was carried out manually, by visually screening 30-min-long signals recorded at all stations and components between May and September 2014. It resulted in the selection of about 1000 potential seismic event records. In a second step, regional events reported by the NORSAR reviewed bulletin (magnitude ≥2.0) or unsupervised generalized beamforming bulletin (NORSAR, 1971) were rejected, leaving 250 potential local events.

Three event types were observed: (1) short-duration signals characterized by distinct *P*- and *S*-wave arrivals associated with local events (Fig. 3a,b), (2) longer-duration signals distinguished by two distinct phases with a temporal separation on the order of 10 s associated with regional events not reported in the previous catalogs (Fig. 3c), and (3) long-duration signals (>100 s or more) associated with source processes that were more difficult to identify and were therefore classified as noise. The first two categories of events were located employing the 1D velocity model extended to larger depths (Fig. S2c,d) and a grid search. They appeared to occur mainly in two areas to the southeast and north of the network, collocated with a coal mine and glaciers (Fig. 1). Using waveform cross-correlation, events were classified into clusters, among which the events to the southeast and north represent two well-correlated families. However, the *P*-wave arrivals of the events located to the southeast in the vicinity of the mine contained more energy at higher frequencies (≤10 Hz; Fig. S4). We noted further that the events located close to the mine were distributed randomly in time, whereas the events located in the north occurred within 15 days in July 2014.

Previous studies of icequakes in Svalbard (e.g., Köhler *et al.*, 2012, 2015) observed a wide variety of seismic signals associated with glaciers. Therefore, although the events to the north can be interpreted as icequakes, we cannot conclusively determine if the seismicity to the southeast represents mining-induced events or icequakes.

Spectral and *f-k* analyses of the ambient seismic noise

To characterize the spectral content of the ambient seismic wavefield, we analyzed data recorded by the SPITS array from 2007 to 2014 in the frequency range between 0.1 and 40 Hz. In a first step, probabilistic power spectral density functions (McNamara *et al.*, 2009) were computed to establish ambient seismic noise baselines: long-term yearly baselines to

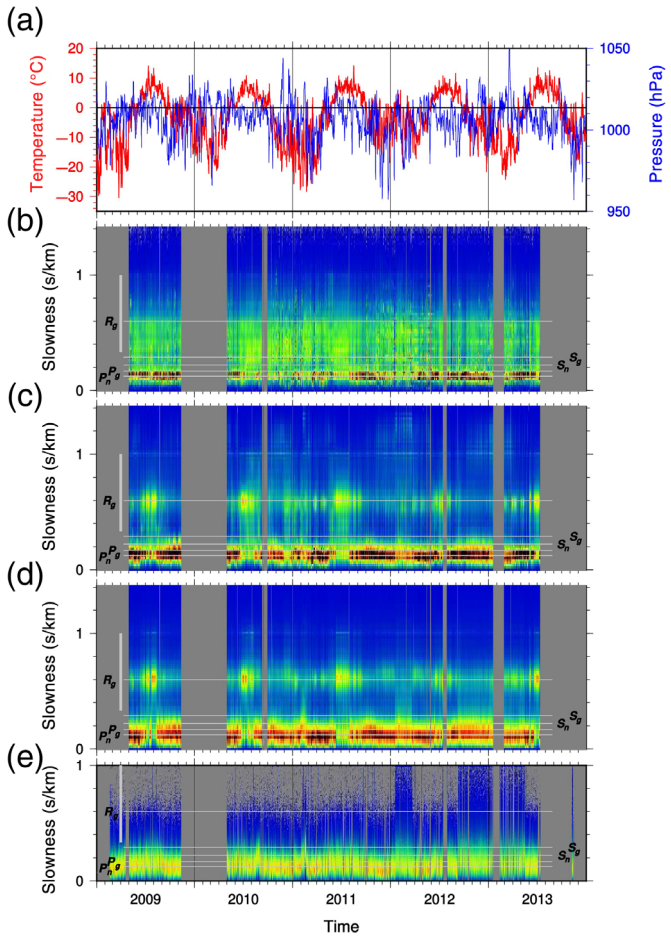

Figure 4. (a) Temperature and air pressure are compared with absolute horizontal slowness from 2009 to 2013 for frequencies (b) 6–18, (c) 3–9, (d) 1.5–4.5, and (e) 0.5–2.0 Hz. Horizontal slowness is presented as histograms for 3 hr intervals. Color scales are relative and not comparable given the choice of window lengths for different frequency bands. Horizontal gray lines mark standard slowness values for local body wave phases (*Pg* ≈ 1/6 s/km, *Pn* ≈ 1/8 s/km, *Sg* ≈ 1/3.5 s/km, *Sn* ≈ 1/4.5 s/km, and *Rg* ≈ 1/1.6 s/km). The color version of this figure is available only in the electronic edition.

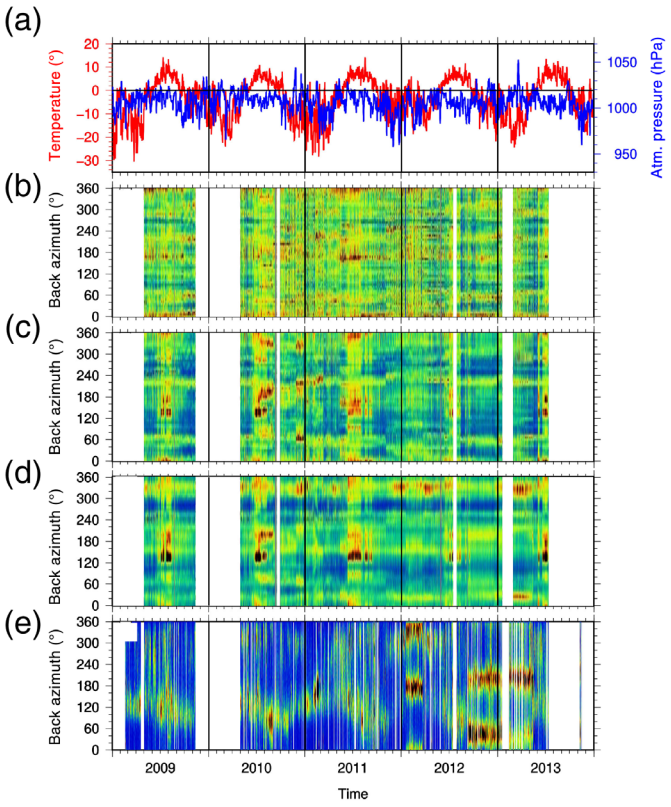

Figure 5. (a) Temperature and air pressure are compared from 2009 to 2013 with backazimuths computed for absolute horizontal slowness filtered in the slowness range from 0.33 to 1 s/km for frequencies (b) 6–18, (c) 3–9, (d) 1.5–4.5, and (e) 0.5–2.0 Hz. Color scales are relative and not comparable given the choice of window lengths for different frequency bands. The color version of this figure is available only in the electronic edition.

characterize ambient noise conditions and short-term weekly as well as monthly baselines to determine changing station performance and noise characteristics (Fig. S5). At frequencies below 0.2 and above 5 Hz, the ambient seismic noise was close to the new low noise model (Petersen, 1993). The maximum energy was present at about 0.2–0.3 Hz, corresponding to the secondary microseism. A stable source of noise was also recovered at 0.5–4 Hz. In addition, seasonal changes occurred in the noise level. At high frequencies (>2 Hz), the level of noise was higher in summer than in winter, which can be explained by the increase in icequake activity due to ice melting (Köhler *et al.*, 2015). By contrast, low-frequency noise was stronger in winter, most likely due to the dynamic weather conditions similar to those described for Norway (Demuth *et al.*, 2016) or to the strong noise source in the northern Atlantic Ocean that dominates during winter (Stehly *et al.*, 2006).

To better characterize the direction in which ambient seismic noise propagates across the array, a frequency–wavenumber (*f*–*k*) technique (Kværna and Ringdahl, 1986; Krim and Viberg, 1996; Rost and Thomas, 2002) was applied in the frequency bands 0.5–2, 1.5–4.5, 3–9, and 6–18 Hz. Lower frequencies were omitted due to the small aperture of the SPITS array and correspondingly limited resolution. The time resolution of the sliding window analysis was adjusted to capture high-frequency transients of both tectonic and cryogenic origin as well as background noise around 1 Hz. For each time window, the following wave-field attributes were recorded: the absolute horizontal slowness, the direction of propagation, the coherency of the wavefield via the multitrace semblance coefficient (Neidell and Taner, 1971), and the beam power.

The overall output of the analysis windows was summarized with histograms for individual wavefield parameters. To resolve diurnal changes, the summary histograms were computed for 3 hr intervals representing the *f*-*k* results from

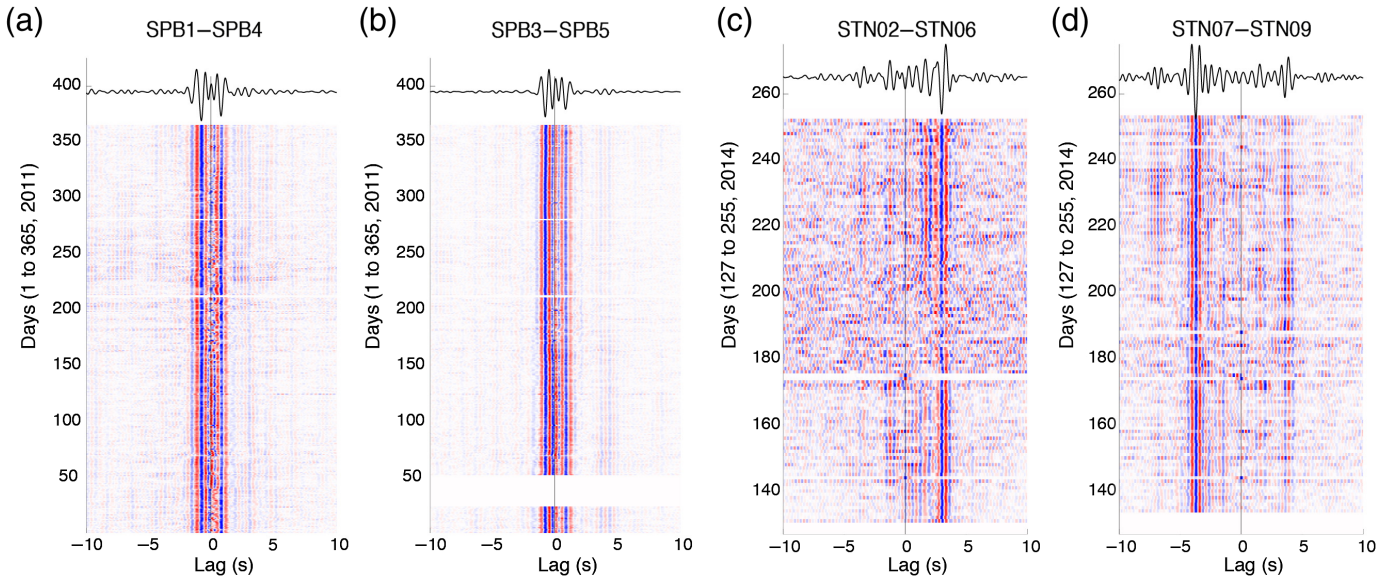

Figure 6. Examples of cross-correlation functions (CCFs) computed from SPITS and SEISVAL data (vertical components) for stations pairs (a) SPB1–SPB4 (north–south direction), (b) SPB3–SPB5 (east–west direction), (c) STN02–STN06 (northwest–southeast direction, north side of Adventdalen), and (d) STN07–STN09 (southeast–northwest direction, south side of Adventdalen). The color version of this figure is available only in the electronic edition.

~3600 time windows (lowest frequency band) to ~108, 000 time windows (highest frequency band).

Figure 4 shows histograms of absolute horizontal slowness values binned in 0.02 s/km and within 3 hr time windows. For all frequency ranges, the histograms peaked at typical *P*- and *S*-wave slownesses of crust and upper mantle. This pattern was a temporally stable feature throughout the years with recurring short-lived interruptions during early summer months when surface-wave propagation velocities became dominant. To investigate this annual pattern, we filtered the analysis results, keeping only time windows showing slownesses in the range from 0.33 to 1 s/km. In Figure 5, we show the resulting back-azimuth distributions of the seasonally dominating surface wavefield (see Fig. S6 for the summer period of 2011). We observed an abrupt change of the back-azimuth pattern of the surface-wave field in the first days of June. Coinciding with the average air temperature rising above the freezing point, the histograms show strong arrivals at several back-azimuths in both the northern and southern directions, the most pronounced being N140°E–N160°E. The directional source concentration persisted for a few weeks. After disappearing for two weeks at the end of the summer, two other activity bursts from southeastern directions were detected. This behavior was visible for all studied years (2010–2013; Fig. 5).

We attribute this consistent seasonal pattern to cryogenic glacier-related seismicity typically being active during summertime, probably due to the effect of increasing temperature promoting cracks within the glacier body and allowing for basal gliding due to melt water accumulating at its base. Köhler *et al.* (2015) reported the occurrence of such concentrated seismicity in the frequency band from 1 to 8 Hz for a large number of glaciers in Svalbard. In particular, during summers and autumns within the years 2007–2013, daily icequake activity was recorded at Kongsfjorden (to the northnorthwest) and Hornsund (to the south). In addition, the analysis of microseismicity in this study features event locations correlated with glaciers around Adventdalen.

Ambient Seismic Noise Cross-Correlation

CCFs computation

Data processing was performed using a Python code developed for dense array noise-correlation studies (Boué *et al.*, 2013, 2014). Daily CCFs were computed separately for the SEISVAL network and the SPITS array.

The SEISVAL network consists of two different types of sensors, so the instrument response had to be homogenized first. Because the Güralp CMG40 instrument response features the wider spectrum, the data recorded by these sensors were corrected to the Noemax Agecodagis instruments instead. Because of the different numbers of components of the SPITS sensors, the analysis of these data focused only on pairs of vertical components.

Data were band-pass filtered between 0.01 and 30 Hz for SPITS and between 0.03 and 40 Hz for SEISVAL. Daily records were split into 6 hr segments for SPITS and into 2 hr segments for SEISVAL. The mean and trend of the time series were removed. A data segment was rejected if its elevated relative energy content suggested contamination with an earthquake or icequake signal. Spectral whitening was applied to the

segments (50–20 s for SPITS, 25–30 Hz for SEISVAL), followed by time-domain clipping at 3.5 times the standard deviation of the amplitude distribution in each time window.

Example normalized daily CCFs are plotted in Figure 6 for the frequency range of 0.5–2 Hz for the whole year of 2011 for SPITS and for days-of-year 127–255 of 2014 for SEISVAL. The abscissa denotes lag time and the ordinate calendar time. The stack over all days is presented at the top of the panels.

Compared with the SEISVAL CCFs, the shorter interstation distances at the SPITS array led to higher signal-to-noise ratios and shorter travel times of the main Rayleigh wave arrival around 0 s lag time, and the correlation coda exhibited stable arrivals that were used for velocity change monitoring. The symmetry of the SPITS CCFs tended to vary seasonally, resulting from variations in the noise source directions (Stehly *et al.*, 2006) as illustrated in the previous section.

The CCFs reconstructed between STN02 and STN06 on the north side of Adventdalen contained a signal at positive lag times, whereas the CCFs between STN07 and STN09 on the south side of Adventdalen featured an arrival at negative lag times. STN06 and STN07 were located to the southeast, whereas STN02 and STN09 were located to the northwest (Fig. 1). The observed asymmetries seem to be a general feature for northwest–southweast-oriented travel paths along the northern and southern edge of the Adventdalen valley, suggesting that at least in the analyzed frequency bands, noise sources were spatially heterogeneous and clustered toward the northwest (compare with fig. 1 in Stehly *et al.*, 2006). For CCF stacks corresponding to travel paths across the valley, the signals were more symmetric compared with the travel paths along the valley. This strongly suggests a predominant energy flux along the valley, which can be explained by the skewed noise source distribution in combination with the topography forming a guide for wave propagation.

Modeling CCFs

To better understand the CCF properties, we modeled wave propagation in Adventdalen. For a diffuse equipartitioned noise field, the nine cross-correlations between pairs of seismograph components are empirical estimates of the corresponding Green's functions (Lobkis and Weaver, 2001; Snieder, 2004; Tsai, 2010).

We employed the 3D velocity model described in the Velocity model building section, combined with a topographic model of the region. The computational domain consisted of a volume of $10 \times 15 \times 3$ km^3 covering the locations of the temporary broadband network stations and the CO_2Lab, with a 3 km margin on all sides to reduce boundary effects. Calculations, carried out using 1024 processors of a supercomputer, were accurate to 9 Hz. Given the minimum shear-wave speed of 660 m/s in the 3D velocity model, this required a grid spacing of 9 m leading to about 6.2×10^8 grid points and a timestep of 0.0012 s/samples for simulation times of 7.5 s. Computations were carried out using the SW4 fourth-order accurate finite-difference code for seismic-wave propagation (Sjögreen and Petersson, 2012; Petersson and Sjögreen, 2015, 2017). We took a reciprocal approach to the calculations (Eisner and Clayton, 2001), placing a source at each station location in turn, while recording at the remaining stations. This entailed three forward runs of the elastic finite-difference model at each of the station locations applying a force in each of the three cartesian directions and recording the six-component strain tensor at each of the other 11 stations.

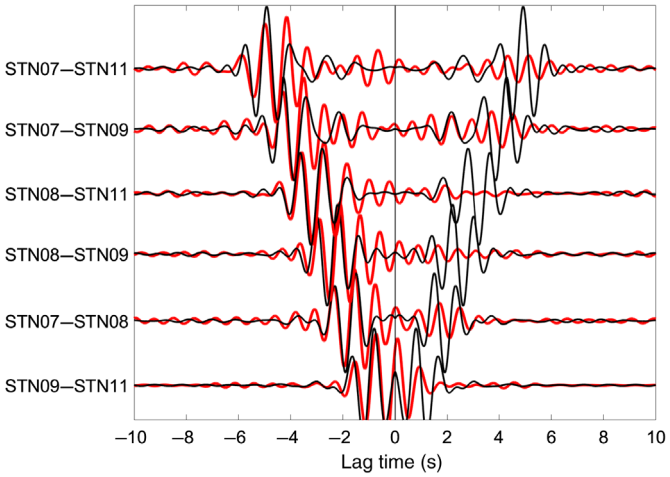

Figure 7. Comparison of modeled Green's functions and recorded CCFs for sensor pairs on the south side of Adventdalen; black lines represent modeled Green's functions, and red lines represent measured cross-correlation stacks; both data filtered within 0.75–1.5 Hz. The color version of this figure is available only in the electronic edition.

Figure 7 compares the modeled Green's functions with the CCF stacks for sensor pairs situated on the south side of Adventdalen by taking the derivative of the latter. For the signals at negative time lags, the agreement between measured and modeled Green's functions was remarkable, providing an independent validation of the 3D velocity model. A similarly good match could be observed for sensor pairs along the north side of Adventdalen for positive lag times and for most of the short travel paths across the valley, that is, for sensor pairs STN06–STN07, STN02–STN09, and STN05–STN08. For the remaining station pairs, especially for the longer propagation paths across the valley, the agreement was not as good. A polarization analysis of the modeled seismograms confirmed the propagating waves as Rayleigh waves.

Seismic Velocity Variation Monitoring

Rayleigh wave sensitivity

We analyzed the sensitivity of Rayleigh waves at depth to changes in shear-wave velocity following Boore and Nafi Toksöz (1969). To this end, we computed derivatives of

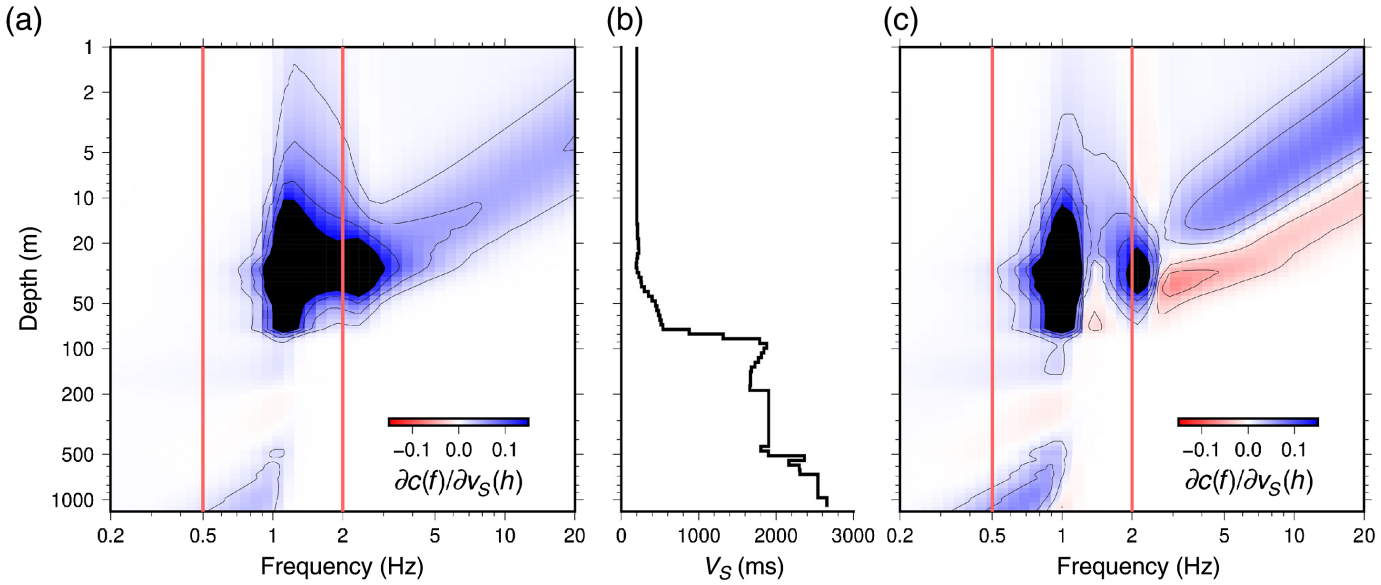

Figure 8. Sensitivity of Rayleigh wave (a) phase and (c) group velocity to changes in shear-wave velocity with depth for (b) 1D velocity model including measured shallow shear-wave velocities; red vertical lines in (a) and (c) mark 0.5–2 Hz frequency band for which velocity variations were observed in the following. Please note logarithmic scale of axes. The color version of this figure is available only in the electronic edition.

fundamental Rayleigh wave phase and group velocity curves for a large frequency band (0.2–20 Hz) in response to changes in *S*-wave velocity within 100 individual layers of increasing thickness up to the model depth of 1200 m (Fig. 8).

As velocity model, we used the extended 1D *S*-wave velocity (Fig. S3c). *P*-wave and density variations were not considered because the sensitivity of surface-wave velocity to *P*-wave velocity and density variations are small compared with that of shear-wave velocity changes (Boore and Nafi Toksöz, 1969). Domains in the frequency–depth plot for which an increase in shear-wave velocity leads to an increase in Rayleigh wave velocities are shown in blue, and an anticorrelated response is indicated in red. White regions show a neutral response. For this shear-wave velocity model, sensitivities of Rayleigh wave phase and group velocities are strongest within the uppermost 100 m. Down to depths of approximately 80 m, where the shear-wave velocity increased abruptly, a change of 1 m/s in shear-wave velocity caused a change of up to 0.2 m/s in Rayleigh wave velocity (for both phase and group velocities), corresponding to a fractional change of 20%.

Velocity changes in permafrost at SPITS

We investigated three years of data for evidence of velocity changes in the subsurface using CCFs computed from all vertical components included in the SPITS array. Prior to the analysis, we removed sporadic low-quality correlations from the three-year gathers. Relative travel-time changes (dt/t) were estimated in the coda of the CCFs to infer a potential relative velocity variation ($dv/v = -dt/t$; e.g., Snieder *et al.*, 2002; Brenguier *et al.*, 2008; Hadziioannou *et al.*, 2009; Hillers *et al.*, 2015). This analysis is typically performed using the time-domain stretching method (Sens-Schönfelder and Wegler, 2006) or the spectral doublet method (Poupinet *et al.*, 1984), also known as the moving window cross-spectral method (MWCS). Both methods were tested and gave similar results. We continue showing the results from the doublet method.

For each station pair, a reference cross-correlation function (RCCF) was constructed using the stack of all daily CCFs over the study period. Subsequently, a ± 10 days moving-average stack of daily CCFs was compared with this RCCF. The MWCS method was applied to the coda of the CCFs at negative and positive lag times between 8 and 20 s. This window starts sufficiently late in the coda after the arrival of the direct surface wave to minimize the influence of ballistic components or azimuthal variations in the distribution of noise sources (Colombi *et al.*, 2014). The final dv/v estimate was obtained by averaging over all station pairs. We investigated different frequency bands but focus here on the results obtained in the 0.5–2 Hz range (Fig. 9). The *f-k* analysis shows higher plane-wave energy arriving at higher frequencies compared with the body wave components or the relative surface-wave energy in this frequency range (Fig. 4). However, the cleaner dv/v measurements are obtained in the target range 0.5–2 Hz, which reflects the comparatively higher coherency of the reconstructed coda waves at these longer periods.

Strong seasonal variations in seismic velocity were resolved with a maximum amplitude of about ± 0.08%, in addition to a linearly decreasing trend (Fig. 9). An anticorrelation between changes in seismic velocity and temperatures measured between 0.5 and 15 m in depth in a nearby borehole (Isaksen

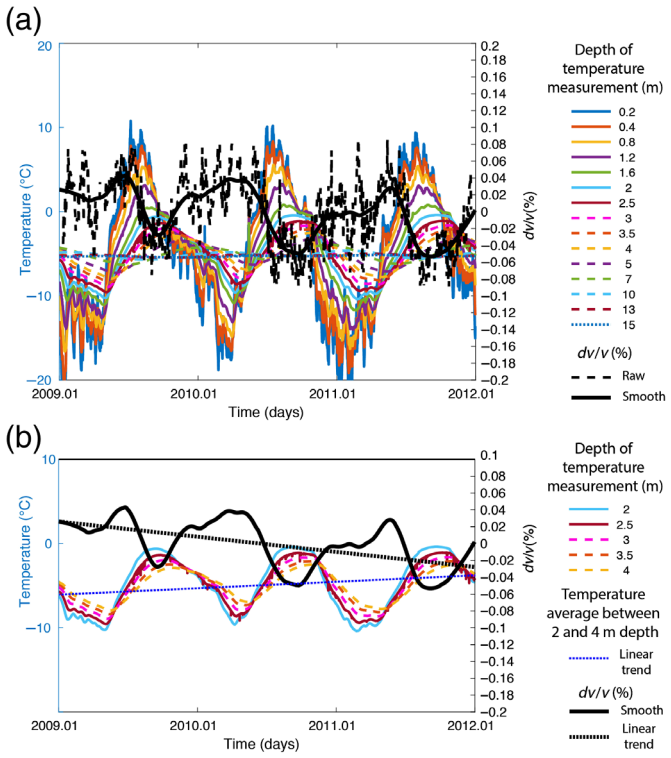

Figure 9. Relative seismic velocity changes compared with ground temperatures. Black solid line represents locally weighted linear regression of *dv/v* estimated with the doublet method for the frequency range 0.5–2 Hz (represented as black dashed line); colored curves represent borehole temperatures measured at different depths (0.2–15 m) within a borehole at Janssonhaugen (denoted JB on Fig. 1; Isaksen *et al.*, 2001, 2007). (a) Temperature from 0.2 to 15 m depth plotted together with *dv/v* (raw and smoothed curves); (b) temperature from 2 to 4 m depth, smoothed *dv/v* and linear velocity and temperature trends computed from the smoothed *dv/v* curve and temperature averaged between 2 and 4 m depth, respectively. The color version of this figure is available only in the electronic edition.

et al., 2001, 2007) is clearly visible. Once the temperatures increased, seismic velocities decreased and vice versa. This anticorrelation was particularly in phase with temperature variations at 2–4 m depth (Fig. 9b).

In the JB borehole close to the SPITS array (Fig. 1), the permafrost and active layer thicknesses are 220 m and 1.5–1.7 m, respectively (Isaksen *et al.*, 2007). Below the active layer and down to ~10 m in depth, the permafrost experiences seasonal temperature fluctuations below the freezing point (Fig. 9; Isaksen *et al.*, 2007). These seasonal temperature changes influence the ice content of the ground, which significantly affects its seismic properties, in particular the shear modulus (e.g., Timur, 1968; Zimmerman and Michael, 1986; LeBlanc *et al.*, 2004; Dou and Ajo-Franklin, 2014; Dou *et al.*, 2016; James *et al.*, 2017, 2019; Stemland *et al.*, 2020). In Alaska, James *et al.* (2017) monitored large velocity changes in the active layer employing the MWCS method based on high-frequency noise recordings (13–17 Hz), resulting in *dv/v* values of up to ~10%. The authors pointed out that the measured amplitudes of *dv/v* were lower than expected for thawing (90%) because only a portion of the wave energy could be recovered.

Ambient seismic noise across the SPITS array exhibited a higher coherency in a lower frequency range compared with the study of James *et al.* (2017), which allowed us to resolve velocity changes at 0.5–2 Hz. The estimated *dv/v* amplitude was lower compared with the observations by James *et al.* (2017) in the active layer. Figure 9 illustrates that the smoothed *dv/v* estimates are in phase and anticorrelated with the temperature variations at 2–4 m in depth. From this, we interpret that the velocity variations observed in the frequency range 0.5–2 Hz are governed by temperature changes below the active layer but above the depth of zero annual mean temperature change at ~10 m depth (Fig. 9b). Temperature and thus velocity variations at this depth level may be explained by ice saturation with the percentage of unfrozen interstitial water drastically affecting the permafrost seismic properties (Zimmerman and Michael, 1986; LeBlanc *et al.*, 2004; Dou and Ajo-Franklin, 2014; Stemland *et al.*, 2020). In particular, the ice saturation is most likely controlled by the degree of salinity of the Adventdalen group geological formation (Stemland *et al.*, 2020). To examine the possibility that spurious *dv/v* measurements may be caused by systematic temporal changes in the wavefield associated with icequake activity, we compared the temporal distributions of events in the NORSAR *f-k* analysis (NORSAR, 1971) with the *dv/v* time series and the temperature variations at 3 m depth (Fig. 10).

The rose plots in Figure 10 suggest that most of the detected events are located in a north–south direction, consistent with the glacier activity described in the previous section and in Köhler *et al.* (2015). The majority of events are characterized by high-frequency content: the number of detections decreases by a factor of 18 between the frequency bands 1–4 and 0.5–2 Hz. In the event count plot, the number of daily detections (normalized over the full 3 yr period) is color coded and compared with the *dv/v* time series filtered in the same frequency bands. In the 1–4 Hz range, a strong increase in the number of events detected during summer is discernible, consistent with an increase in icequake activity. However, significant seasonal *dv/v* variations are absent. In contrast, the low-frequency results exhibiting the strongest seasonal *dv/v* variations show much less icequake activity.

These results are thus not implying a correlation between icequake activity or wavefield anatomy and seismic velocity change estimates. We conclude that the preprocessing of CCFs, especially the removal of segments containing large-amplitude transients, resulted in a sufficiently randomized coda wavefield in the 8–20 s analysis window and thus unbiased *dv/v* estimates

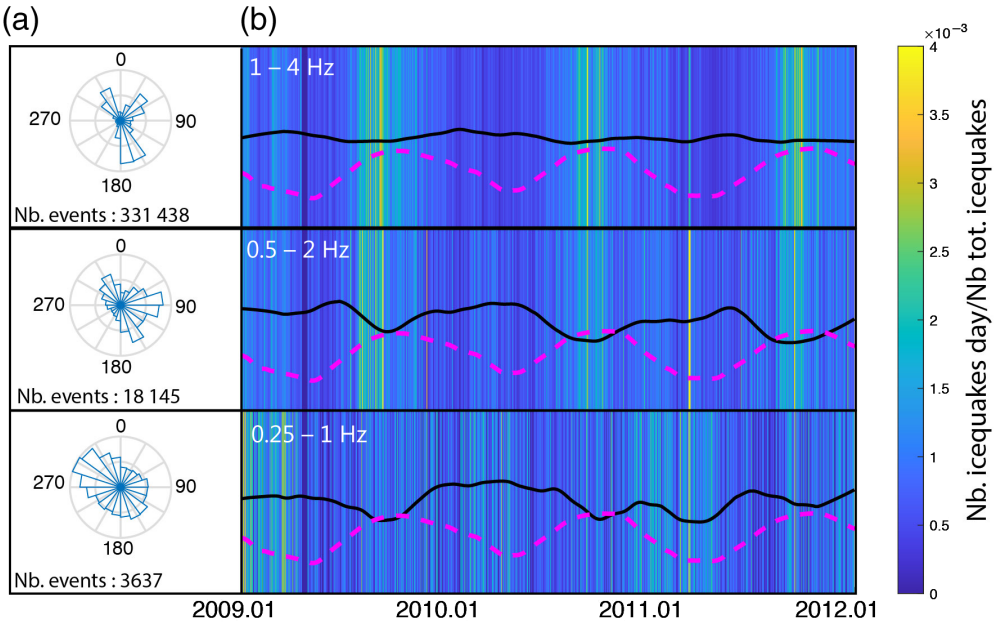

Figure 10. (a) Rose plots indicating azimuthal distributions of events according to their dominant frequency for the years 2009–2011. The absolute number of detected events in each frequency range is indicated below each rose plot. (b) Number of high-frequency events (icequakes) per day normalized over the whole time period (see color bar) compared with *dv/v* estimates (black lines) and temperature measured at 3 m depth variations (magenta dashed lines). From top to bottom: frequency ranges of 1–4, 0.5–2, and 0.25–1 Hz. The color version of this figure is available only in the electronic edition.

(Hillers *et al.*, 2015). Ballistic components with a dominant ~north–south propagation direction in summer associated with the icequake activity did not govern the results. We conclude that the obtained change in the elastic properties of the medium are genuine and most likely driven by changes in temperature.

Therefore, we consider the SPITS continuous array data to be an important resource to study the behavior of the permafrost layer in response to the globally increasing temperature associated with climate change. We demonstrated the ability to study the impact of the seasonal temperature variation on permafrost. We also highlight the resolution of a long-term effect that is illustrated by the consistency between the decreasing trend in *dv/v* and a simultaneous increase in temperatures from 2009 to 2011 observed in the Janssonhaugen borehole (Fig. 9). This type of analysis would benefit from ambient seismic noise measurements within shallower surface layers, requiring the installation of additional sensors with reduced interstation distances. Such a network could be accommodated readily within the aperture limits of the current array, in which essential infrastructure in terms of cables and communication lines is already provided. Independent laboratory analysis of Adventdalen permafrost samples also would be of great interest to better quantify the effect of ice saturation on the observed seismic velocity variations (e.g., Zimmerman and Michael, 1986).

Conclusions

Most of the challenges in the application of geophysical investigations in polar environments are related to extreme seasonal changes as well as the permafrost cover (Kneisel *et al.*, 2008). On the one hand, these climate conditions induce large variations in the elastic properties of the ground, allowing for testing of new methodologies in these natural laboratories. On the other hand, the deployment of monitoring systems is hampered by these environmental settings. The installation of a seismic monitoring network within the Adventdalen valley is challenging. First, the long duration of the winter period with snow and ice coverage means that there is only a limited time window available in which deployment and maintenance of instruments is feasible. Second, options for instrument installations are limited, which in turn may result in a network geometry that is not optimal for a specific research target. For example, the SEISVAL broadband seismometers could not be installed on the valley plain, but had to be placed on its north and south sides because a broad braided river emerges during summertime. It is unknown in which seismic frequency range this braided river contributes to the ambient seismic noise field. Only a few rock outcrops were available onto which seismometers could be cemented, and these boulders are not connected to the bedrock, which increases the possibility of low-quality records. The stiffness of the frozen ground prevented burial of the seismometers to shield them from wind. Although the construction of a permanent network such as SPITS is costly and challenging, it is essential for proper long-term seismic monitoring of geological features such as permafrost. In particular, the array geometry allows for an enhanced signal-to-noise ratio employing array analysis approaches. The deployment of temporary seismic networks is essential as well because their geometry and thus sensitivity can be adapted to a specific target. In addition, they complement the permanent station coverage. This study demonstrates that passive seismic data acquired over an extended period of time and collected for initially different purposes can be used for environmental applications, such as monitoring the

temporal evolution of shallow permafrost layers and thus helping to assess its vulnerability to climate change.

Our study emphasizes the necessity of combining different monitoring and analysis methods. The results from the various approaches demonstrate the feasibility of geophysical methods for continuous permafrost monitoring. The observations provide suggestions for future seismological investigations and highlight the sensitivities and resolution capabilities of the employed methods. We demonstrated that seismic interferometry applied to several years of continuous data can resolve permafrost dynamics. Specifically, we recovered both seasonal and long-term temperature effects on the permafrost through the measurement of seismic velocity variations.

The main results of our study are:

- A shallow *S*-wave velocity model of the subsurface representative of late summer conditions was built from active seismic data. The model is characterized by low shear-wave velocities of only 200 m/s within the upper 50 m, increasing to approximately 450 m/s at 100 m depth.
- The temporary SEISVAL network and the permanent SPITS array are suitable for detection and identification of local microseismic events. Detected seismicity consists of icequakes and probably mining-induced events.
- Spectral analysis of the ambient seismic noise recorded at SPITS shows that the energy is dominated by the secondary microseism peak. A stable noise source is also recovered at 0.5–4 Hz.
- An *f-k* analysis performed on five years of SPITS data (2009–2013) shows that energy corresponding to typical *P*- and *S*-wave slownesses dominates over all frequency ranges. Interestingly, this pattern seems to be a temporally stable feature throughout each year, reduced in visibility only during summer months when surface-wave velocities prevail.
- This transition between wave types occurs very suddenly, coinciding with the average air temperature exceeding the freezing point and is accompanied by a change in wavefield direction.
- The CCFs computed between SEISVAL stations was successfully modeled based on a 3D velocity model of the Adventdalen valley.
- The wavefield observed in the modeled Green's functions fits Rayleigh waves propagating along the length of Adventdalen.
- Seasonal changes in seismic velocity extracted from SPITS array data appear to be correlated with temperature variations in the permafrost below the active layer.
- A decreasing trend in seismic velocity within the shallow permafrost layer is interpreted as the effect of an increase in the average temperature recorded at Svalbard between 2009 and 2011.

Data and Resources

The Norwegian Seismic Array (NORSAR) bulletins are available at https://www.norsar.no/seismic-bulletins/. The 12 seismic stations for the SEISVAL experiment were rented from the French national pool of portable seismic instruments SisMob-RESIF (https://sismob.resif.fr/). We used a high-performance Python code developed at ISTerre, Université Grenoble Alpes, to compute the noise-correlation functions (Boué *et al.*, 2013, 2014). The 3D Adventdalen velocity model was updated by systematic gathering of all existing data and their evaluation using the OpendTect freeware (https://dgbes.com/index.php/software/free#opendtect). The open-source sw4 code is available at https://github.com/geodynamics/sw4. A part of the plots was made using the Generic Mapping Tools version 6.1.1 (Wessel and Smith, 1998). The supplemental material including additional figures is available to the reader. The information about Global Land Ice Measurements from Space (GLIMS) is available at http://www.glims.org. All websites were last accessed in May 2021.

Declaration of Competing Interests

The authors acknowledge that there are no conflicts of interest recorded.

Acknowledgments

This work was financed by the Research Council of Norway Grant Number 224880 (SafeCO_2 II project). The project was sponsored additionally by industry partners Lundin, RWE DEA Norge, and Statoil (now Equinor). The first version of the 3D Adventdalen velocity model was developed in a previous project, similarly funded by the Research Council of Norway (Grant Number 189994, SafeCO_2 project) and industry partners Lundin, Octio, READ, ConocoPhillips, and Statoil (now Equinor). Further, the authors would like to thank the Norwegian Metacenter for Computational Science (NOTUR) for granting them computation time on their supercomputer Abel to compute 3D waveform propagation within Adventdalen (Synth CO_2 project). The authors offer their heartfelt thanks to the Longyearbyen CO_2Lab managed by the University Centre in Svalbard (UNIS) CO_2Lab AS for help and support provided throughout the years. The authors thank K. Isaksen for giving them access to borehole temperature data; S. Sikora, G. Sauvin, P. Zhao, N. Skøyen, and P. Lavadera Lubrano for their help on the field; F. Brenguier, M. Campillo, A. Köhler, M. Roth, and J. Schweitzer for helpful discussions related to this study; L. Zühlsdorff and E. V. Bergfjord for translating the Adventdalen reservoir model into a NORSAR3D velocity model; and V. Oye for participation in and active support of the project and review of the article. The authors are thankful to the guest editors M. Pirli and P. Voss as well as two anonymous reviewers who provided comments that greatly improved the article.

References

Anisimov, O. A. (2007). Potential feedback of thawing permafrost to the global climate system through methane emission, *Environ. Res. Lett.* **2,** no. 4, 045016, 7.

Bergh, S. G., A. Braathen, and A. Andresen (1997). Interaction of basement-involved and thin-skinned tectonism in the tertiary fold-thrust belt of central Spitsbergen, Svalbard, *AAPG Bull.* **81,** no. 4, 637–661.

Bælum, K., T. Johansen, H. Johnsen, K. Rød, B. O. Ruud, and A. Braathen (2012). Subsurface structures of the Longyearbyen CO_2 Lab study area in Central Spitsbergen (Arctic Norway), as mapped by reflection seismic data, *Norw. J. Geol.* **92,** no. 4, 377–389.

Boore, D., and M. Nafi Toksöz (1969). Rayleigh wave particle motion and crustal structure, *Bull. Seismol. Soc. Am.* **9,** no. 1, 331–346.

Boué, P., P. Poli, M. Campillo, H. Pedersen, X. Briand, and P. Roux (2013). Teleseismic correlations of ambient seismic noise for deep global imaging of the Earth, *Geophys. J. Int.* **194,** 844–848.

Boué, P., P. Roux, M. Campillo, and X. Briand (2014). Phase velocity tomography of surface waves using ambient noise cross correlation and array processing, *J. Geophys. Res.* **119,** no. 1, 519–529.

Braathen, A., K. Bælum, H. H. Christiansen, T. Dahl, O. Eiken, H. Elvebakk, F. Hansen, T. H. Hanssen, M. Jochmann, T. A. Johansen, *et al.* (2012). The Longyearbyen CO_2 Lab of Svalbard, Norway – Initial assessment of the geological conditions for CO_2 sequestration, *Norw. J. Geol.* **92,** no. 4, 353–376.

Brenguier, F., N. M. Shapiro, M. Campillo, V. Ferrazzini, Z. Duputel, O. Coutant, and A. Nercessian (2008). Towards forecasting volcanic eruptions using seismic noise, *Nat. Geosci.* **1,** no. 2, 126–130.

Bungum, H., A. Alsaker, L. B. Kvamme, and R. A. Hansen (1991). Seismicity and seismotectonics of Norway and nearby continental shelf areas, *J. Geophys. Res.* **96,** no. B2, 2249–2265.

Christiansen, H., B. Etzelmüller, K. Isaksen, H. Juliussen, H. Farbrot, O. Humlum, M. Johansson, T. Ingeman-Nielsen, L. Kristensen, J. Hjort, *et al.* (2010). The thermal state of permafrost in the Nordic area during the International Polar Year 2007–2009, *Permafr. Periglac. Process.* **21,** no. 2, 156–181.

Colombi, A., J. Chaput, F. Brenguier, G. Hillers, P. Roux, and M. Campillo (2014). On the temporal stability of the coda of ambient noise correlations, *C. R. Geosci.* **346,** 307–316.

Crawford, J. M., W. E. N. Doty, and M. R. Lee (1960). Continuous signal seismograph, *Geophysics* **25,** no. 1, 95–105.

Demuth, A., L. Ottemöller, and H. Keers (2016). Ambient noise levels and detection threshold in Norway, *J. Seismol.* **20,** no. 3, 889–904.

Dou, S., and J. B. Ajo-Franklin (2014). Full-wavefield inversion of surface waves for mapping embedded low-velocity zones in permafrost, *Geophysics* **79,** no. 6, EN107–EN124.

Dou, S., S. Nakagawa, D. Dreger, and J. Ajo-Franklin (2016). A rock-physics investigation of unconsolidated saline permafrost: P-wave properties from laboratory ultrasonic measurements, *Geophysics* **81,** no. 1, WA233–WA245.

Eisner, L., and R. W. Clayton (2001). A reciprocity method for multiple-source simulations, *Bull. Seismol. Soc. Am.* **91,** no. 3, 553–560.

Hadziioannou, C., E. Larose, O. Coutant, P. Roux, and M. Campillo (2009). Stability of monitoring weak changes in multiply scattering media with ambient noise correlation: Laboratory experiments, *J. Acoust. Soc. Am.* **125,** no. 6, 3688–3695.

Harris, D., J. Albaric, B. Goertz-Allmann, D. Kühn, S. Sikora, and V. Oye (2017). Interference suppression by adaptive cancellation in a high arctic seismic experiment, *Geophysics* **82,** no. 4, V201–V209.

Hillers, G., Y. Ben-Zion, M. Campillo, and D. Zigone (2015). Seasonal variations of seismic velocities in the San Jacinto fault area observed with ambient seismic noise, *Geophys. J. Int.* **202,** no. 2, 920–932.

Humlum, O., A. Instanes, and J. Sollid (2003). Permafrost in Svalbard: A review of research history, climatic background and engineering challenges, *Polar Res.* **22,** no. 2, 191–215.

Isaksen, K., P. Holmlund, J. L. Sollid, and C. Harris (2001). Three deep Alpine-permafrost boreholes in Svalbard and Scandinavia, *Permafr. Periglac. Process.* **12,** no. 1, 13–25.

Isaksen, K., J. L. Sollid, P. Holmlund, and C. Harris (2007). Recent warming of mountain permafrost in Svalbard and Scandinavia, *J. Geophys. Res.* **112,** F02S04, doi: 10.1029/2006JF000522.

James, S. R., H. A. Knox, R. E. Abbott, and E. J. Screaton (2017). Improved moving window cross-spectral analysis for resolving large temporal seismic velocity changes in permafrost, *Geophys. Res. Lett.* **44,** no. 9, 4018–4026.

James, S. R., H. A. Knox, R. E. Abbott, M. P. Panning, and E. J. Screaton (2019). Insights into permafrost and seasonal active-layer dynamics from ambient seismic noise monitoring, *J. Geophys. Res.* **124,** no. 7, 1798–1816.

Kneisel, C., C. Hauck, R. Fortier, and B. Moorman (2008). Advances in geophysical methods for permafrost investigations, *Permafr. Periglac. Process.* **19,** no. 2, 157–178.

Köhler, A., and C. Weidle (2019). Potentials and pitfalls of permafrost active layer monitoring using the HVSR method: A case study in Svalbard, *Earth Surf. Dynam.* **7,** no. 1, 1–16.

Köhler, A., A. Chapuis, C. Nuth, J. Kohler, and C. Weidle (2012). Autonomous detection of calving-related seismicity at Kronebreen, Svalbard, *Cryosphere* **6,** 393–406.

Köhler, A., C. Nuth, J. Schweitzer, C. Weidle, and S. J. Gibbons (2015). Regional passive seismic monitoring reveals dynamic glacier activity on Spitsbergen, Svalbard, *Polar Res.* **34,** no. 1, 26178, doi: 10.3402/polar.v34.26178.

Krim, H., and M. Viberg (1996). Two decades of array signal processing research: The parametric approach, *IEEE Signal Process. Mag.* **13,** no. 4, 67–94.

Kühn, D., V. Oye, J. Albaric, D. Harris, G. Hillers, A. Braathen, and S. Olaussen (2014). Preparing for CO_2 storage in the Arctic – Assessing background seismic activity and noise characteristics at the CO_2 Lab site, Svalbard, *Energy Procedia* **63,** 4313–4322.

Kula, D., D. Olszewska, W. Dobiński, and M. Glazer (2018). Horizontal-to-vertical spectral ratio variability in the presence of permafrost, *Geophys. J. Int.* **214,** no. 1, 219–231.

Kværna, T., and F. Ringdahl (1986). Stability of various f-k estimation techniques, *NORSAR Semiannual Tech. Summary 1-86/87*, 29–40, doi: 10.21348/p.1986.0001.

LeBlanc, A., R. Fortier, M. Allard, C. Cosma, and S. Buteau (2004). Seismic cone penetration test and seismic tomography in permafrost, *Can. Geotech. J.* **41,** no. 5, 796–813.

Lehujeur, M., J. Vergne, J. Schmittbuhl, D. Zigone, A. Le Chenadec, and E. Team (2018). Reservoir imaging using ambient noise correlation from a dense seismic network, *J. Geophys. Res.* **123,** no. 8, 6671–6686.

Lobkis, O., and R. Weaver (2001). On the emergence of the Green's function in the correlations of a diffuse field, *J. Acoust. Soc. Am.* **110,** no. 6, 3011–3017.

Lubrano Lavadera, P., D. Kühn, B. Dando, I. Lecomte, K. Senger, and Å. Drottning (2018). CO_2storage in the high Arctic: Efficient modelling of pre-stack depth-migrated seismic sections for survey planning, *Geophys. Prospect.* **66,** no. 6, 1180–1200.

McNamara, D., C. Hutt, L. Gee, H. M. Benz, and R. Buland (2009). A method to establish seismic noise baselines for automated station assessment, *Seismol. Res. Lett.* **80,** no. 4, 628–637.

Mykkeltveit, S., A. Dahle, J. Fyen, T. Kværna, P. Larsen, R. Paulsen, F. Ringdal, and I. K. Bungum (1992). Extensions of the Northern Europe Regional Array Network—New small-aperture arrays at Apatity, Russia, and on the Arctic island of Spitsbergen, *NORSAR*

Semiannual Tech. Summary I-92/93, 58–71, doi: 10.21348/p.1992.0001.

Neidell, N., and M. Taner (1971). Semblance and other coherency measures for multichannel data, *Geophysics* **36,** no. 3, 482–497.

NORSAR (1971). NORSAR seismic bulletins, doi: 10.21348/b.0001.

Olaussen, S., K. Senger, A. Braathen, S. Grundvåg, and A. Mørk (2019). You learn as long as you drill; research synthesis from the Longyearbyen CO_2 Laboratory, Svalbard, Norway, *Norw. J. Geol.* **99,** 157–181.

Oye, V., A. Braathen, and U. Polom (2013). Preparing for CO_2 storage at the Longyearbyen CO_2 Lab: Microseismic monitoring of injection tests, *First Break* **31,** 95–101.

Oye, V., H. Gharti, D. Kühn, and A. Braathen (2010). Microseismic monitoring of fluid injection at the Longyearbyen CO_2 Lab, Svalbard, *Cahiers du Centre européen de géodynamique et de séismologie* **30,** 109–114.

Petersen, J. (1993). Observations and modeling of seismic background noise, *U.S. Geol. Surv. Open-File Rept. 93-322*, Albuquerque, New Mexico, 42 pp.

Petersson, N. A., and B. Sjögreen (2015). Wave propagation in anisotropic elastic materials and curvilinear coordinates using a summation-by-parts finite difference method, *J. Comput. Phys.* **299,** 820–841.

Petersson, N. A., and B. Sjögreen (2017). User's guide to SW4, version 2.0, *Lawrence Livermore National Laboratory Tech. Report LLNL-SM-741439*.

Pirli, M. (2013). NORSAR system responses manual, Third Ed., *NORSAR Tech. Rept.,* 304 pp., doi: 10.21348/p.2013.0001.

Pirli, M., J. Schweitzer, and B. Paulsen (2013). The Storfjorden, Svalbard, 2008–2012 aftershock sequence: Seismotectonics in a polar environment, *Tectonophysics* **601,** 192–205.

Polom, U. (2006). Vibration generator for seismic applications, *U.S. Patent 7136325b2*, available at https://patents.google.com/patent/US7136325 (last accessed May 2021).

Polom, U., G. Druivenga, E. Grossmann, S. Grüneberg, and W. Rode (2011). Transportabler Scherwellenvibrator: Deutsches Patent und Markenamt, *Patentschrift DE10327757B4* (in German).

Polom, U., L. Hansen, G. Sauvin, J.-S. L'Heureux, I. Lecomte, C. M. Krawczyk, M. Vanneste, and O. Longva (2010). High-resolution SH-wave seismic reflection for characterization of onshore ground conditions in the Trondheim harbor, Central Norway, in *Advances in Near-surface Seismology and Ground-penetrating Radar*, R. D. Miller, J. D. Bradford, and K. Holliger (Editors), SEG, Tulsa, 297–312, doi: 10.1190/1.9781560802259.ch18.

Poupinet, G., W. L. Ellsworth, and J. Frechet (1984). Monitoring velocity variations in the crust using earthquake doublets: An application to the Calaveras Fault, California, *J. Geophys. Res.* **89,** no. B7, 5719–5731.

Raup, B., A. Racoviteanu, S. Khalsa, C. Helm, R. Armstrong, and Y. Arnaud (2007). The GLIMS geospatial glacier database: A new tool for studying glacier change, *Global Planet. Change* **56,** 101–110.

Rost, S., and C. Thomas (2002). Array seismology: Methods and applications, *Rev. Geophys.* **40,** no. 3, 2-1–2-27.

Roux, P., M. Wathelet, and A. Roueff (2011). The San Andreas Fault revisited through seismic-noise and surface-wave tomography, *Geophys. Res. Lett.* **38,** no. 13, L13319, doi: 10.1029/2011GL047811.

Schaefer, K., H. Lantuit, V. E. Romanovsky, E. A. G. Schuur, and R. Witt (2014). The impact of the permafrost carbon feedback on global climate, *Environ. Res. Lett.* **9,** no. 8, 085003, doi: 10.1088/1748-9326/9/8/085003.

Schweitzer, J., A. Köhler, and J. M. Christensen (2021). Development of the NORSAR network over the last 50 years, *Seismol. Res. Lett.* doi: 10.1785/0220200375.

Seneviratne, S., M. Donat, A. Pitman, R. Knutti, and R. L. Wilby (2016). Allowable CO_2 emissions based on regional and impact-related climate targets, *Nature* **529,** 477–483.

Senger, K., J. Tveranger, A. Braathen, S. Olaussen, K. Ogata, and L. Larsen (2014). CO_2 storage resource estimates in unconventional reservoirs: Insights from a pilot-sized storage site in Svalbard, Arctic Norway, *Environ. Earth Sci.* **73,** no. 8, 3987–4009.

Sens-Schönfelder, C., and U. Wegler (2006). Passive image interferometry and seasonal variations of seismic velocities at Merapi Volcano, Indonesia, *Geophys. Res. Lett.* **33,** no. 21, L21302, doi: 10.1029/2006GL027797.

Shapiro, N. M., and M. Campillo (2004). Emergence of broadband Rayleigh waves from correlations of the ambient seismic noise, *Geophys. Res. Lett.* **31,** no. 7, L07614, doi: 10.1029/2004GL019491.

Shapiro, N. M., M. Campillo, L. Stehly, and M. H. Ritzwoller (2005). High-resolution surface-wave tomography from ambient seismic noise, *Science* **307,** no. 5715, 1615–1618.

Sjögreen, B., and N. A. Petersson (2012). A fourth order accurate finite difference scheme for the elastic wave equation in second order formulation, *J. Sci. Comput.* **52,** no. 1, 17–48.

Snieder, R. (2004). Extracting the Green's function from the correlation of coda waves: A derivation based on stationary phase, *Phys. Rev. E* **69,** no. 4, 046610, doi: 10.1103/PhysRevE.69.046610.

Snieder, R., A. Grêt, H. Douma, and J. Scales (2002). Coda wave interferometry for estimating nonlinear behavior in seismic velocity, *Science* **295,** no. 5563, 2253–2255.

Stehly, L., M. Campillo, and N. Shapiro (2006). A study of the seismic noise from its long-range correlation properties, *J. Geophys. Res.* **111,** no. B10306, doi: 10.1029/2005JB004237.

Stemland, H. M., T. Johansen, and B. O. Ruud (2020). Potential use of time-lapse surface seismics for monitoring thawing of the terrestrial Arctic, *Appl. Sci.* **10,** no. 5, 1875, doi: 10.3390/app10051875.

Timur, A. (1968). Velocity of compressional waves in porous media at permafrost temperatures, *Geophysics* **33,** no. 4, 584–595.

Tsai, V. (2010). The relationship between noise correlation and the Green's function in the presence of degeneracy and the absence of equipartition, *Geophys. J. Int.* **182,** no. 3, 1509–1514.

Wessel, P., and W. H. F. Smith (1998). New, improved version of generic mapping tools released, *Eos Trans. AGU* **79,** 579–579.

Westermann, S., U. Wollschläger, and J. Boike (2010). Monitoring of active layer dynamics at a permafrost site on Svalbard using multi-channel ground-penetrating radar, *The Cryosphere* **4,** no. 4, 475–487.

Williams, P., and M. Smith (1989). *The Frozen Earth: Fundamentals of Geocryology*, Cambridge University Press, Cambridge, doi: 10.1017/CBO9780511564437.

Zimmerman, R. W., and S. K. Michael (1986). The effect of the extent of freezing on seismic velocities in unconsolidated permafrost, *Geophysics* **51,** no. 6, 1285–1290.

Manuscript received 18 December 2020
Published online 7 July 2021